

A constraint on the carbon-climate feedback factor over the northern high latitude forests

Junjie Liu (✉ junjie.liu@jpl.nasa.gov)

Jet Propulsion Laboratory, Caltech <https://orcid.org/0000-0002-7184-6594>

Paul Wennert

California Institute of Technology

Article

Keywords:

Posted Date: May 12th, 2022

DOI: <https://doi.org/10.21203/rs.3.rs-1609995/v1>

License:   This work is licensed under a Creative Commons Attribution 4.0 International License.

[Read Full License](#)

1
2 **A constraint on the carbon-climate feedback factor over the northern high latitude forests**

3
4 **Junjie Liu^{1,2*}, Paul O. Wennberg^{2*}**

5
6 **1. Jet Propulsion Laboratory, Caltech, USA**

7 **2. Caltech, USA**

8
9 The high latitude land (>50°N) is warming at more than twice the rate of the rest of globe. In spite
10 of a broad consensus that the warming over the high latitudes northern forests (HLNF) has
11 enhanced photosynthesis and contributed to the greening trend^{1,2}, quantifying what the impact of
12 temperature increase on photosynthesis and greenness has been difficult due to the concurring
13 influence of the CO₂ fertilization effect³. Here, using an ensemble of biogeochemical models from
14 the Trends in Net Land Atmosphere Carbon Exchange project (TRENDY), we identified an
15 emergent relationship between the spatial sensitivity of both gross primary productivity (GPP) and
16 greenness (Leaf Area Index, LAI) to temperature and their corresponding temporal changes due
17 to warming - the so-called carbon-climate feedback factor γ . Using spatially-resolved observations
18 of GPP and LAI, we estimated the sensitivity of GPP and LAI increase due to temperature to be -
19 $18.3 \pm 2.6\%/^{\circ}\text{C}$ and $27.8 \pm 4.3\%/^{\circ}\text{C}$ respectively. These observationally-derived sensitivities are
20 $\sim 50\%$ and $\sim 100\%$ larger, respectively, than those diagnosed from the ensemble of TRENDY
21 models. We estimated that the regional mean GPP increased $24 \pm 3.7\%$ between 2006-2015 and
22 1983-1992, much larger than the $5 \pm 1.3\%$ increase from the CO₂ fertilization effect implied by
23 Wenzel et al.⁴. Taken together with the CO₂ fertilization effect estimated by⁴, our results help
24 resolve the partition of the competing effect between CO₂ fertilization and warming on plants
25 growth over the HLNF, and help reduce the uncertainties in predictions. Our results also highlight
26 the dramatic changes of terrestrial biosphere caused by historical warming over the region. An
27 important implication of this work is that uptake of carbon as temperatures continue to warm is
28 likely to continue providing significant buffering of atmospheric CO₂ increase.

29
30 *Correspondence to: junjie.liu@jpl.nasa.gov; wennberg@caltech.edu

31

32 Temperature over the northern hemisphere (NH) high latitudes ($>50^{\circ}\text{N}$) has been increasing at
33 more than twice the rate of the rest of the globe, and given the continuing increases in greenhouse
34 gases, this trend is unlikely to slow in the foreseeable future (IPCC AR6). Concurrently, ground
35 and satellite observations have illustrated dramatic changes in terrestrial biosphere activity: longer
36 growing season^{5,6}, a greening trend over the majority of the region^{1,7-10}, and an increase of CO_2
37 seasonal cycle amplitude and net carbon uptake from the atmosphere^{2,11-14}. One of the fundamental
38 processes that drive these changes is photosynthesis: a process that converts light energy into
39 chemical energy through electron transport, which is used to fix atmosphere carbon into organic
40 carbon compounds through carboxylation¹⁵. The maximum rate of both electron transport and
41 carboxylation increases exponentially with temperature before an optimal temperature for plants
42 growth is reached^{16,17}. The mean growing season temperature over land $>50^{\circ}\text{N}$ is between 5 -
43 18°C (Extended Data Fig. 1), less than the optimal growth temperature for plants even accounting
44 for acclimation and adaptation^{18,19}. Thus, the increase in temperature has been proposed as a
45 mechanism that drives the increase of photosynthesis over the region^{2,11,20}. However, diagnosing
46 the extent to which temperature enhances plants growth is complicated by the co-occurring
47 elevated CO_2 that enhances photosynthesis through increasing the CO_2 gradient between the
48 ambient air and intercellular spaces within leaves^{21,22}, the so called “ CO_2 fertilization” effect²³.

49
50 The CO_2 fertilization and warming effect on photosynthesis are relatively well-understood at leaf
51 level¹⁷, but are uncertain when integrated up to canopy scale. Consequently, the current state-of-
52 science terrestrial biogeochemical models (TBMs) show a large range of the response of
53 photosynthesis to climate change and CO_2 increase, the so-called γ and β effects, respectively^{3,24}.
54 As a result, the uncertainty in the simulated net carbon uptake is close to 100% over the high
55 latitudes²⁵. The accuracy of historical simulations and future predictions of ecosystem carbon
56 uptake strongly depends on our understanding of both the γ and β effects²⁴. A few past studies
57 derived empirical emergent relationships between observables and model simulations of the
58 carbon-climate feedback factor γ over the tropics²⁶⁻²⁸ and the β effect over high latitudes or at
59 global scale^{29,30}, and then used observations to constrain γ and β over these regions. However,
60 quantitative impact of temperature increases on plants growth over high latitudes (the γ effect) is
61 still elusive and is anticipated to be distinct from that in the tropics due to the large climatological
62 differences³¹. Over the tropics, increasing temperature reduces the terrestrial biosphere net carbon

63 uptake from the atmosphere, causing positive carbon-climate feedbacks²⁶, while over the high
64 latitudes, warming trend invigorates plants growth, acting as a negative feedback to the climate³¹.
65 The predictions of future climate change critically depend on understanding of this negative
66 carbon-climate feedbacks.

67

68 Here we expose an emergent relationship based on the outputs from an ensemble of TBMs, and
69 use observations to constrain the impact of temperature increase (the γ effect) on the changes of
70 gross primary production (GPP) and greenness over the high latitude northern forest (HLNF). It is
71 complementary to the tropical carbon-climate feedback factor proposed by Cox et al.²⁶ and the β
72 effect on GPP over temperate and boreal forest derived by Wenzel et al.³⁰. The emergent
73 relationship derived here is based on an earlier study¹² which introduced a framework to use
74 photosynthetic responses to spatial temperature gradients to infer temporal changes in
75 photosynthesis. We extend that framework to derive an emergent relationship between the model-
76 simulated spatial sensitivity of photosynthesis and greenness to temperature and their temporal
77 changes driven by the changing climate. We then use the observed spatial sensitivity of GPP and
78 greenness and the derived emergent relationship to constrain their temporal changes due to
79 temperature increase over the high latitudes.

80

81 **Spatial sensitivity of GPP and greenness to temperature**

82 If the temporal changes of GPP and greenness caused by temperature are strongly correlated with
83 their corresponding spatial sensitivity to temperature, the simulated spatial sensitivity of GPP and
84 greenness to temperature from each model should be stable with time. Thus, we first evaluated the
85 temporal consistency of the simulated spatial sensitivities of GPP and greenness to temperature
86 from current earth system biogeochemical models. We examined both Leaf Area Index (LAI) and
87 GPP from an ensemble of TBMs from the Trends in Net Land Atmosphere Carbon Exchange
88 project (TRENDY) v6, and simulations where only CO₂ was varied (S1) and simulations where
89 both CO₂ and climate were varied (S2). LAI tracks the one-sided green leaf area per unit of ground
90 surface area; GPP is a function of both the absorption of photosynthetically active radiation (APAR)
91 (related to greenness) and light use efficiency. The quantity APAR is not analyzed here since it is
92 not available from TRENDY output. Analyzing both GPP together with LAI, however, allows us

93 to understand the contributions of both greenness and light use efficiency to the sensitivity of GPP
94 to temperature.

95

96 Since the S1 runs are driven by a 20-year repeating climatology, we calculated 20-year mean GPP
97 and LAI starting at 1901 to remove the impact of climate on GPP and LAI changes in S1 runs.
98 Each group has 10-year overlap (e.g., 1901-1920, 1911-1930, etc.) to increase the sample size. In
99 the end, we had 11 groups each for S1 and S2 runs from each model. We selected those grids (>
100 50°N) with at least 40% tree cover fraction (Extended Data Table 1), and then fitted an exponential
101 curve between the growing season (GS) mean temperature (GS-T) and growing season GPP and
102 LAI for each group from each model (Methods). We selected 40% as a threshold to remove those
103 grids with dominant grassland and cropland vegetation types, since water availability could be
104 dominant climate driver over these vegetation types³². The coefficient of the exponential fit is
105 taken as the spatial sensitivity of GPP and LAI to the GS-T, while the R^2 (GPP or LAI, T) shows
106 how strong the spatial distributions of GS GPP and LAI are coupled with the GS-T in each model.
107 The standard deviation of the fitting coefficients among the 11 groups in each model shows the
108 stability of the spatial sensitivity of GPP and LAI to GS-T with time.

109

110 While observations show a strong spatial coherence between GS-T and both GPP and LAI
111 (Extended Data Figs. 2 and 3), the models show a large range of coupling strength, ranging from
112 no relationship at all ($R^2=0$) to strong coupling ($R^2=0.7$) (Figures 1 and Extended Data Table 1).
113 In our further analysis, we only selected those models with R^2 larger than 0.2 for either LAI-T or
114 GPP-T relationship, and the models that have monthly LAI and GPP output. In total, there are
115 eight models that pass the criteria (Extended Data Table 1). Among these eight models, despite its
116 large variations in the coupling strength, the magnitude of the spatial sensitivity of GPP and LAI
117 to temperature remains relatively stable with time within any single model for both S1 and S2 runs
118 (Figure 1 and Extended Data Figure 4). For example, the spatial sensitivity of GS-LAI to GS-T of
119 model A only ranges 0.19 $\text{m}^2/\text{m}^2/^\circ\text{C}$ to 0.21 $\text{m}^2/\text{m}^2/^\circ\text{C}$ among the 11 groups (Figure 1). For each
120 model, the spatial sensitivity of GPP and LAI to temperature is similar between S1 and S2 runs
121 (Figure 1 and Extended Data Fig. 4), indicating that the spatial sensitivity of GPP and LAI to
122 temperature is an intrinsic model characteristic that reflects the distinctive model structure in each
123 model.

124

125 The TRENDY models underestimate the spatial sensitivity of both GPP and LAI to temperature
126 compared to the observations (Figure 1). We used the OCO-2 SIF, three FLUXCOM GPP products
127 and three LAI products to calculate the spatial sensitivity of observed GPP and LAI to temperature
128 (Methods). The mean spatial sensitivity of GS-LAI to GS-T from the TRENDY models is $0.10 \pm$
129 $0.07 \text{ m}^2/\text{m}^2/^\circ\text{C}$, ~60% lower than the spatial sensitivity of the observed LAI to temperature (0.16
130 $\pm 0.02 \text{ m}^2/\text{m}^2/^\circ\text{C}$). The mean spatial sensitivity of GPP to temperature in the TRENDY models is
131 $0.11 \pm 0.04 \text{ gC}/\text{m}^2/\text{day}/^\circ\text{C}$, only half of the sensitivity of the observed GPP to temperature (0.22
132 $\pm 0.03 \text{ gC}/\text{m}^2/\text{day}/^\circ\text{C}$). Only two models have larger spatial sensitivity of LAI to temperature than
133 the observed value. All the eight models underestimate the spatial sensitivity of GPP to
134 temperature, with model A the closest to the spatial sensitivity of the SIF-constrained GPP to
135 temperature.

136

137 **Emergent constraint on change in GPP and LAI due to T increase**

138 The fact that the spatial sensitivity to temperature is nearly invariant with time in the TRENDY
139 simulations (Figure 1 and Extended Data Fig. 4) implies that the LAI and GPP would simply shift
140 to higher values as temperature increases following the relationship defined by the spatial
141 sensitivity if nothing else changes. This indicates that the sensitivity derived from the observed
142 spatial dependence of GPP and LAI on temperature can be used as an emergent constraint on how
143 warming will drive changes in GPP and LAI.

144

145 Figure 2A and 2B shows the spatial sensitivity of LAI and GPP, respectively, to temperature vs.
146 the corresponding temporal sensitivity to temperature only (Methods) during the growing season
147 (Methods). The models with larger spatial sensitivity to temperature also predict larger percentage
148 increase of GPP and LAI with increasing temperature. The large R^2 values (0.94 and 0.79
149 respectively) between the spatial sensitivity of LAI and GPP to growing season temperature and
150 the corresponding temporal sensitivity to temperature suggest that there is an emergent relationship
151 between them. Thus, the observed spatial sensitivity of GPP and LAI to temperature can provide
152 an emergent constraint on the carbon-climate feedback factor γ over the HLNF.

153

154 Based on the linear relationship derived from the TRENDY models (Figure 2A and 2B) and the
155 constraint provided by the observed spatial sensitivity of LAI and GPP to temperature, LAI
156 increased $18.3 \pm 2.6\%/^{\circ}\text{C}$ and GPP increased $27.8 \pm 4.3\%/^{\circ}\text{C}$, which are $\sim 50\%$ and $\sim 100\%$ higher
157 than the TRENDY model mean (Figure 2C and 2D). The significant underestimation of the
158 sensitivity of plants growth to temperature over the high latitudes may have contributed to the
159 weaker carbon sink simulated by these models^{14,33}. The emergent constraint reduces the
160 uncertainty of estimated LAI and GPP temporal sensitivity by 70% and 24% respectively. The
161 uncertainty of emergent constraint includes uncertainties in the observed spatial sensitivity to
162 temperature, the linear fitting between the spatial sensitivity to temperature and the temporal
163 sensitivity to temperature (Methods). The smaller uncertainty reduction in the estimated GPP
164 temporal sensitivity is due to the relatively larger uncertainty compared to LAI in both of these
165 two aspects. In calculating the probability function for the models, we assume equal possibilities
166 of each model. The observed carbon climate feedback factor γ_{obs}^{GPP} is much larger than the
167 magnitude of γ_{obs}^{LAI} , because GPP is a function of both greenness and LUE. LUE also increases
168 with temperature exponentially¹², contributing to the additional sensitivity of GPP to temperature
169 upon the sensitivity of greenness to temperature. It implies that only accounting for the sensitivity
170 of greenness to temperature would underestimate the spatial sensitivity of GPP to temperature.
171 The fact that the γ_G^{GPP} has similar magnitude as γ_G^{LAI} in the TRENDY models indicates these
172 models underestimate the sensitivity of light use efficiency to temperature.

173

174

175 The growing season mean temperature increased more than 0.4°C over most of the Eurasia and
176 northern NA between 2006-2015 and 1983-1992, with the Eurasia having larger temperature
177 increase than NA (Figure 3). The observation-constrained carbon-climate feedback factors γ_{obs}^{LAI}
178 and γ_{obs}^{GPP} implies that such temperature increase contributed to 9-27% increase of LAI and 12-35%
179 increase in GPP over most of the region (Figure 3). The percentage increases in LAI and GPP are
180 especially large over the high latitudes of Eurasia, where the growing season mean temperature
181 and the magnitude of LAI and GPP are lower (Extended Data Fig. 1 and Fig. 5). On average, the
182 regional mean LAI increased $14 \pm 2.0\%$ based on the γ_{obs}^{LAI} , comparable to 16% increase based on
183 NOAA AVHRR LAI product, but much larger than the GIMMS AVHRR LAI product (Figure 3
184 and Extended Data Fig. 5). The regional mean GPP increased $24 \pm 3.7\%$ based on γ_{obs}^{GPP} , which is

185 much larger than the impact of CO₂ fertilization effect implied by Wenzel et al. ³⁰; based on
186 Wenzel et al., the GPP increased 5 ± 1.3 % over the high latitude from the 40 parts per million
187 (ppm) CO₂ increase during this time period (Methods). The dominant warming effect on enhancing
188 plants growth over high latitudes is consistent with Forkel et al².

189

190 The emergent constraint described in this study indicates that the TRENDY models significantly
191 underestimate the impact of historical temperature increase on greenness and GPP over the HLNF,
192 which may have contributed to the much weaker net carbon sink simulated by these models
193 compared to the top-down atmosphere flux inversion results. Taken together with Wenzel et al³⁰.,
194 our results help resolve the partition of the competing effect between CO₂ fertilization and
195 warming over the HLNF, providing a unique metric to improve process representation in the
196 models and reduce uncertainties in quantifying carbon-climate feedback factors over the HLNF.
197 Our study unambiguously shows that increasing temperature is the dominant factor that drives the
198 GPP increase and the historical greening trend over HLNF. As temperature over the HLNF
199 continues to increase at much higher rate than the rest of the globe it is critical to monitoring how
200 greenness and photosynthesis are changing and to be on alert to any tipping point where increasing
201 temperatures no longer act as negative feedbacks to climate. In the absence of such a tipping point,
202 uptake of carbon by the HLNF as temperatures continue to warm is likely to continue providing
203 significant buffering of atmospheric CO₂ increase from anthropogenic emissions and other positive
204 carbon-climate feedback processes.

205

206

207 **Methodology**

208 **1. Growing season definition**

209 In each of the 20-year group of the S1 and S2 runs, we first calculated the monthly climatology of
210 GPP from each TRENDY model. Based on the monthly climatology during each time span, we
211 defined growing season at each model grid as the time period when GPP is larger than 20% of the
212 maximum *GPP* at that grid. We chose 20% threshold here to reduce the impact of errors of the
213 observational-constrained GPP at low values (section 2). We only chose those grids that have
214 well-defined spring (20% to 80% of maximum GPP before maximum GPP) and fall season (20%
215 to 80% of maximum GPP after maximum GPP) that have at least three samples to calculate
216 growing season mean value. At last, we chose those grids that have at least 40% tree cover and
217 have valid definition of growing season throughout the whole time period. (Table S1). Note that
218 the grids for each model are the same set of grid points throughout the time period, but could differ
219 among the models. The length of the growing season could also change.

220

221 **2. GPP and LAI observations**

222 In this study, we used four GPP products and three LAI products to calculate the observationally-
223 constrained spatial sensitivity of GPP and LAI to temperature. These four GPP products are OCO-
224 2 SIF constrained GPP¹² and three FluxCom GPP products that are based on different neural
225 network algorithms³⁴. We fitted an exponential function between the spatial distribution of
226 growing season GPP and growing season T for each product (Figure S3). The SIF-constrained
227 GPP gives the highest sensitivity (0.25 ± 0.02 gC/m²/day/°C). The three different FluxCom GPP
228 products have the sensitivities of 0.22 ± 0.02 , 0.20 ± 0.02 , and 0.15 ± 0.02 gC/m²/day/°C. The
229 mean spatial sensitivity of GPP to temperature across the four products is 0.21 ± 0.04 , which was
230 used here to define the observationally-constrained spatial sensitivity of GPP to temperature. The
231 uncertainty includes the uncertainty in both the exponential fitting and the standard deviation
232 among the four products.

233

234 The three LAI products are GIMMS LAI3g³⁵, GIMMS MODIS-LAI³⁶, and NOAA AVHRR
235 products. Following the same procedure as GPP, we fitted an exponential function between the
236 spatial distribution of growing season LAI and growing season T for each product (Figure S4).

237 The two AVHRR products have the same spatial sensitivity of $0.15 \pm 0.02 \text{ m}^2/\text{m}^2/ \text{ }^\circ\text{C}$, and the
 238 MODIS LAI has the spatial sensitivity of $0.17 \pm 0.02 \text{ m}^2/\text{m}^2/ \text{ }^\circ\text{C}$. The mean spatial sensitivity of
 239 LAI to temperature is then $0.16 \pm 0.02 \text{ m}^2/\text{m}^2/ \text{ }^\circ\text{C}$ and is used as our observationally-constrained
 240 sensitivity of LAI to temperature.

241

242 We regridded all the data to $4^\circ \times 5^\circ$ grid to reduce sampling errors, especially the SIF-constrained
 243 GPP products. But as shown in ¹², the spatial sensitivity is similar between $1^\circ \times 1^\circ$ and $4^\circ \times 5^\circ$
 244 resolution.

245

246 3. Carbon-climate feedback factors from TRENDY models

247 We define carbon-climate feedback factor γ as the percentage change of interested carbon fluxes
 248 (GPP) or state (LAI) per degree Celsius change in temperature:

$$249 \gamma = \left(\frac{\Delta g}{\Delta T}\right)_T \quad (1)$$

250 where

$$251 \Delta g = \left[\left(\frac{g_n - g_0}{g_0}\right)\right] \quad (2)$$

252 The symbols g_n and g_0 represent growing season GPP or LAI at year t_n and t_0 .

253 To calculate carbon-climate feedback factor γ from TRENDY simulations, we used both S1 and
 254 S2 runs. The S1 runs have time-varying CO_2 concentration, but repeat the 1901-1920 climate every
 255 20 years. The S2 runs have time-varying CO_2 and climate. Thus, the total changes of carbon fluxes
 256 or carbon state g in S2 runs can be written as:

257

$$258 \left(\frac{\Delta g}{\Delta T}\right)_{S2} = \left(\frac{\Delta g}{\Delta T}\right)_{S1} + \gamma \quad (8)$$

259

260 We can calculate $\left(\frac{\Delta g}{\Delta T}\right)_{S2}$ and $\left(\frac{\Delta g}{\Delta T}\right)_{S1}$ from the S2 and S1 runs, and the carbon-climate feedback
 261 factor γ is then just the difference between $\left(\frac{\Delta g}{\Delta T}\right)_{S2}$ and $\left(\frac{\Delta g}{\Delta T}\right)_{S1}$. Equation (8) can also be written as:

$$262 \gamma = \left(\frac{(\Delta g)_{S2} - (\Delta g)_{S1}}{\Delta T}\right) \quad (9)$$

263

264 To calculate the right-hand side of equation (9), we assume that the temporal changes of GPP and
265 LAI follow a similar exponential relationship as the spatial sensitivity to temperature but with the
266 possibility of different coefficients:

$$267 \quad g = a \exp(bT) \quad (10)$$

268 The changes of g can be written as:

$$269 \quad \log(g_n) - \log(g_0) = a_n - a_1 + b(T_n - T_0) \quad (11)$$

270 Equation (3) can be further written as:

$$271 \quad \log\left(\frac{g_n}{g_0}\right) = a_n - a_1 + b(T_n - T_0) \quad (12)$$

272 So the temporal sensitivity of GPP or LAI to temperature can be written as:

$$273 \quad \frac{[\log(\frac{g_n}{g_0})]}{\Delta T} = b \quad (13)$$

274 Equation (13) can be further written as:

275

$$276 \quad \frac{[(\frac{g_n - g_0}{g_0})]}{\Delta T} = \frac{[(\Delta g)]}{\Delta T} = \exp(b) - 1 \quad (14)$$

277

278 We derived b with linear fitting between $\log(g_n) - \log(g_0)$ and $(T_n - T_0)$ from S1 and S2 runs
279 of each model. The carbon-climate feedback factor γ is then the difference between $\exp(b)_{S2}$ and
280 $\exp(b)_{S1}$. We calculated growing season mean GPP or LAI every 20 years with 10-year overlap
281 from 1901 to 2010 to remove the impact of time-varying T on S1 runs and also ensure enough
282 sample size. Then, we calculated Δg relative to the mean between 1901-1920.

283 4. Calculation of the GPP increase between 2006-2015 and 1983-1992 due to CO_2 increase
284 based on Wenzel et al.³⁰

285 We first calculated the mean annual CO_2 concentration over these two time periods using the data
286 available at https://gml.noaa.gov/webdata/ccgg/trends/co2/co2_annmean_gl.txt, and found that
287 the mean CO_2 concentration over these two time periods was 390.0 and 349.8ppm respectively.
288 We then calculated the difference to get the CO_2 change. As Wenzel et al.³⁰ derived that the GPP
289 over the high latitude increase $37 \pm 9\%$ with doubling of CO_2 concentration, we calculated the GPP
290 increase due to the CO_2 increase according to $(390-349.8)/349.8 \times 37$. We calculated the uncertainty
291 as $(390-349.8)/349.8 \times 9$.

292

293

294 Reference:

- 295 1. Keenan, T. F. & Riley, W. J. Greening of the land surface in the world's cold regions
296 consistent with recent warming. *Nat. Clim. Chang.* **8**, 825–828 (2018).
- 297 2. Forkel, M. *et al.* <div xmlns="http://www.w3.org/1999/xhtml">Enhanced seasonal CO₂
298 exchange caused by amplified plant productivity in northern ecosystems</div>. *Science*
299 (80-). **351**, 696–699 (2016).
- 300 3. Bastos, A. *et al.* Contrasting effects of \chem{CO_2} fertilization, land-use change and
301 warming on seasonal amplitude of Northern Hemisphere \chem{CO_2} exchange. *Atmos.*
302 *Chem. Phys.* **19**, 12361–12375 (2019).
- 303 4. Wenzel, S., Cox, P. M., Eyring, V. & Friedlingstein, P. Projected land photosynthesis
304 constrained by changes in the seasonal cycle of atmospheric CO₂. *Nature* **538**, 499–501
305 (2016).
- 306 5. Zeng, H., Jia, G. & Epstein, H. Recent changes in phenology over the northern high
307 latitudes detected from multi-satellite data. *Environ. Res. Lett.* **6**, 45508 (2011).
- 308 6. Ziska, L. *et al.* Recent warming by latitude associated with increased length of ragweed
309 pollen season in central North America. *Proc. Natl. Acad. Sci.* **108**, 4248–4251 (2011).
- 310 7. Park, H., Jeong, S. & Peñuelas, J. Accelerated rate of vegetation green-up related to
311 warming at northern high latitudes. *Glob. Chang. Biol.* **26**, 6190–6202 (2020).
- 312 8. Myneni, R. B., Keeling, C. D., Tucker, C. J., Asrar, G. & Nemani, R. R. Increased plant
313 growth in the northern high latitudes from 1981 to 1991. *Nature* **386**, 698–702 (1997).
- 314 9. Zhu, Z. *et al.* Greening of the Earth and its drivers. **6**, 791–796 (2016).
- 315 10. Piao, S., Friedlingstein, P., Ciais, P., Zhou, L. & Chen, A. Effect of climate and CO₂
316 changes on the greening of the Northern Hemisphere over the past two decades. **33**, 2–7
317 (2006).
- 318 11. Graven, H. D. *et al.* Supplementary Materials for Northern Ecosystems Since 1960.
319 (2013). doi:10.1126/science.1239207
- 320 12. Liu, J., Wennberg, P. O., Parazoo, N. C., Yin, Y. & Frankenberg, C. Observational
321 Constraints on the Response of High-Latitude Northern Forests to Warming. *AGU Adv.* **1**,
322 e2020AV000228 (2020).
- 323 13. Lian, X. *et al.* Summer soil drying exacerbated by earlier spring greening of northern
324 vegetation. *Sci. Adv.* **6**, eaax0255 (2020).
- 325 14. Ciais, P. *et al.* Five decades of northern land carbon uptake revealed by the
326 interhemispheric CO₂ gradient. *Nature* **568**, 221–225 (2019).
- 327 15. Fleming, G. R. & Grondelle, R. van. The Primary Steps of Photosynthesis. *Phys. Today*
328 **47**, 48–55 (1994).
- 329 16. Warren, C. R. & Dreyer, E. Temperature response of photosynthesis and internal
330 conductance to CO₂: results from two independent approaches. *J. Exp. Bot.* **57**, 3057–
331 3067 (2006).
- 332 17. Farquhar, G. D., von Caemmerer, S. & Berry, J. A. A biochemical model of
333 photosynthetic CO₂ assimilation in leaves of C₃ species. *Planta* **149**, 78–90 (1980).
- 334 18. Yamori, W., Hikosaka, K. & Way, D. A. Temperature response of photosynthesis in C₃,
335 C₄, and CAM plants: temperature acclimation and temperature adaptation. *Photosynth.*
336 *Res.* **119**, 101–117 (2014).
- 337 19. Hikosaka, K., Ishikawa, K., Borjigidai, A., Muller, O. & Onoda, Y. Temperature
338 acclimation of photosynthesis: mechanisms involved in the changes in temperature

- 339 dependence of photosynthetic rate. *J. Exp. Bot.* **57**, 291–302 (2006).
- 340 20. Keenan, T. F. & Riley, W. J. Greening of the land surface in the world’s cold regions
341 consistent with recent warming. *Nat. Clim. Chang.* **8**, 825–828 (2018).
- 342 21. Ainsworth, E. A. & Rogers, A. The response of photosynthesis and stomatal conductance
343 to rising [CO₂]: mechanisms and environmental interactions. 258–270 (2007).
344 doi:10.1111/j.1365-3040.2007.01641.x
- 345 22. Deeter, M. N., Martínez-Alonso, S., Andreae, M. O. & Schlager, H. Satellite-Based
346 Analysis of CO₂ Seasonal and Interannual Variability Over the Amazon Basin. *J. Geophys.*
347 *Res. Atmos.* **123**, 5641–5656 (2018).
- 348 23. Long, S. P., Ainsworth, E. A. & Long, S. P. What have we learned from 15 years of free-
349 air CO₂ enrichment (FACE)? A meta-analytic review of the responses of
350 photosynthesis , canopy properties and plant production to rising CO₂. (2004).
- 351 24. Friedlingstein, P. *et al.* Climate – Carbon Cycle Feedback Analysis : Results from the C4
352 MIP Model Intercomparison. *J. Clim.* **19**, (2006).
- 353 25. Keenan, T. F. & Williams, C. A. The Terrestrial Carbon Sink. *Annu. Rev. Environ.*
354 *Resour.* **43**, 219–243 (2018).
- 355 26. Cox, P. M. *et al.* constrained by carbon dioxide variability. *Nature* 1–5
356 doi:10.1038/nature11882
- 357 27. Sullivan, M. J. P. *et al.* Long-term thermal sensitivity of Earth ’ s tropical forests. **874**,
358 869–874 (2020).
- 359 28. Barkhordarian Kevin W and Cressie, Noel and Jewell, Jeffrey and Liu, Junjie, A. and B.
360 Emergent constraints on tropical atmospheric aridity–carbon feedbacks and the future of
361 carbon sequestration. *Environ. Res. Lett.* (2021).
- 362 29. Keenan, T. F. *et al.* A constraint on historic growth in global photosynthesis due to
363 increasing CO₂. *Nature* **600**, 253–258 (2021).
- 364 30. Wenzel, S., Cox, P. M., Eyring, V. & Friedlingstein, P. Projected land photosynthesis
365 constrained by changes in the seasonal cycle of atmospheric CO₂. *Nature* **538**, 499–501
366 (2016).
- 367 31. Yoshikawa, C., Kawamiya, M., Kato, T., Yamanaka, Y. & Matsuno, T. Geographical
368 distribution of the feedback between future climate change and the carbon cycle. *J.*
369 *Geophys. Res.* **113**, (2008).
- 370 32. Liu, D. *et al.* Increasing climatic sensitivity of global grassland vegetation biomass and
371 species diversity correlates with water availability. *New Phytol.* **230**, 1761–1771 (2021).
- 372 33. Friedlingstein, P. *et al.* Global Carbon Budget 2019. *Earth Syst. Sci. Data* **11**, 1783–1838
373 (2019).
- 374 34. Jung, M. *et al.* Scaling carbon fluxes from eddy covariance sites to globe : synthesis and
375 evaluation of the FLUXCOM approach. 1343–1365 (2020).
- 376 35. Zhu, Z. *et al.* Global Data Sets of Vegetation Leaf Area Index (LAI)_{3g} and Fraction of
377 Photosynthetically Active Radiation (FPAR)_{3g} Derived from Global Inventory Modeling
378 and Mapping Studies (GIMMS) Normalized Difference Vegetation Index (NDVI)_{3g} for
379 the Period 1981 to 2011. *Remote Sens.* **5**, 927–948 (2013).
- 380 36. Chen, C. *et al.* China and India lead in greening of the world through land-use
381 management. *Nat. Sustain.* **2**, 122–129 (2019).
- 382 37. Zeng, N., Mariotti, A. & Wetzel, P. Terrestrial mechanisms of interannual CO₂
383 variability. *Global Biogeochem. Cycles* **19**, (2005).
- 384 38. Krinner, G. *et al.* A dynamic global vegetation model for studies of the coupled

385 atmosphere-biosphere system. *Global Biogeochem. Cycles* **19**, (2005).
386 39. Guimberteau, M. *et al.* ORCHIDEE-MICT (v8.4.1), a land surface model for the high
387 latitudes: model description and validation. *Geosci. Model Dev.* **11**, 121–163 (2018).
388 40. Jain, A. K., Meiyappan, P., Song, Y. & House, J. I. CO₂ emissions from land-use change
389 affected more by nitrogen cycle, than by the choice of land-cover data. *Glob. Chang. Biol.*
390 **19**, 2893–2906 (2013).
391 41. Melton, J. R. & Arora, V. K. Competition between plant functional types in the Canadian
392 Terrestrial Ecosystem Model (CTEM) v.~2.0. *Geosci. Model Dev.* **9**, 323–361 (2016).
393 42. Reick, C. H., Raddatz, T., Brovkin, V. & Gayler, V. Representation of natural and
394 anthropogenic land cover change in MPI-ESM. *J. Adv. Model. Earth Syst.* **5**, 459–482
395 (2013).
396 43. Keller, K. M. *et al.* 20th-century changes in carbon isotopes and water-use efficiency:
397 tree-ring-based evaluation of the CLM4.5 and LPX-Bern models. *Biogeosciences* **14**,
398 2641–2673 (2017).
399 44. Clark, D. B. *et al.* The Joint UK Land Environment Simulator (JULES), model description
400 – Part 2: Carbon fluxes and vegetation dynamics. *Geosci. Model Dev.* **4**, 701–722 (2011).
401 45. Sitch, S. *et al.* Evaluation of ecosystem dynamics, plant geography and terrestrial carbon
402 cycling in the LPJ dynamic global vegetation model. *Glob. Chang. Biol.* **9**, 161–185
403 (2003).
404 46. Smith, B. *et al.* Implications of incorporating N cycling and N limitations on primary
405 production in an individual-based dynamic vegetation model. *Biogeosciences* **11**, 2027–
406 2054 (2014).
407 47. Kato, E., Kinoshita, T., Ito, A., Kawamiya, M. & Yamagata, Y. Evaluation of spatially
408 explicit emission scenario of land-use change and biomass burning using a process-based
409 biogeochemical model. *J. Land Use Sci.* **8**, 104–122 (2013).
410 48. Haverd, V. *et al.* A new version of the CABLE land surface model (Subversion revision
411 r4601) incorporating land use and land cover change, woody vegetation demography, and
412 a novel optimisation-based approach to plant coordination of photosynthesis. *Geosci.*
413 *Model Dev.* **11**, 2995–3026 (2018).
414 49. Tian, H. *et al.* North American terrestrial CO₂ uptake largely offset by CH₄ and N₂O
415 emissions: toward a full accounting of the greenhouse gas budget. *Clim. Change* **129**,
416 413–426 (2015).
417

418 **Acknowledgments**

419 We want to thank James Randerson, Dave Schimel, and TRENDY modelers (Stephen Sitch,
420 Pierre Friedlingstein, Vivek Arora, Atul Jain, Markus Kautz, Danica Lobardozzi, Sebastian
421 Lienert, Julia Nabel, Benjamin Poulter, Nicolas Vuichard, Andy Wiltshire, and Ning Zeng) for
422 their comments and suggestions in preparing this paper. We also want to thanks Dr. Ranga Myneni
423 and Dr. Martin Jung for providing the GIMMS and FLUXCOM data. Resources supporting this
424 work were provided by the NASA High-End Computing (HEC) Program through the NASA
425 Advance Supercomputing (NAS) division at Ames Research Center.

426 **Data availability**

427 All data used to support the findings of this study are publicly available. TRENDY model
428 simulations and its met drivers are available on request from TRENDY coordinator Dr. S. Sitch
429 (s.a.sitch@exeter.ac.uk). The GIMMS AVHRR and MODIS LAI data are available upon request
430 from by Dr. Ranga Myneni (rmyneni@bu.edu). The NOAA AVHRR LAI data is available at:
431 <https://www.ncei.noaa.gov/access/metadata/landing->
432 [page/bin/iso?id=gov.noaa.ncdc:C01559](https://www.ncei.noaa.gov/access/metadata/landing-). The FLUXCOM GPP dataset was obtained from
433 <https://www.bgc-jena.mpg.de/geodb/projects/Data.php>. The OCO-2 SIF data is publicly
434 available at
435 [https://disc.gsfc.nasa.gov/datasets/OCO2_L2_Lite_SIF_10r/summary?keywords=oco2%20sif%20](https://disc.gsfc.nasa.gov/datasets/OCO2_L2_Lite_SIF_10r/summary?keywords=oco2%20sif%20lite)
436 [0lite](https://disc.gsfc.nasa.gov/datasets/OCO2_L2_Lite_SIF_10r/summary?keywords=oco2%20sif%20lite)

437 **Funding:**

438 Part of the research was carried out at the Jet Propulsion Laboratory, California Institute of
439 Technology, under a contract with the National Aeronautics and Space Administration,
440 (80NM0018D0004).

441 **Author contributions:**

442 Conceptualization and methodology: JL

443 Investigation: JL and POW

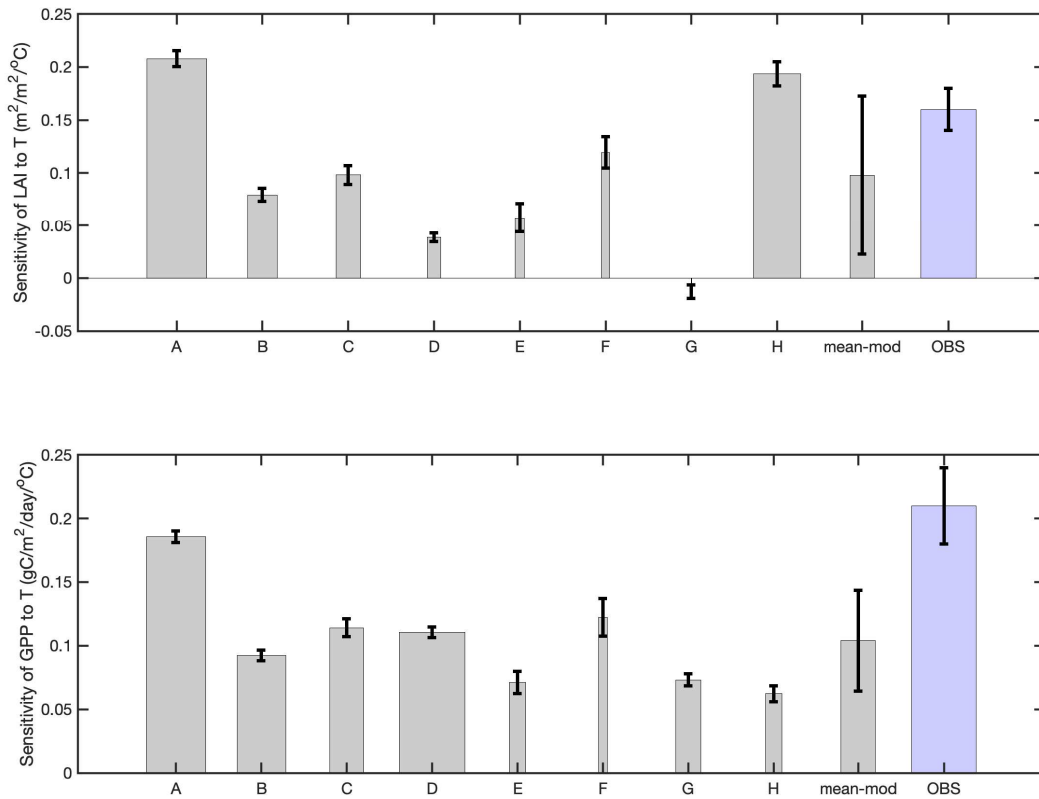
444 Visualization: JL

445 Writing—original draft: JL and POW

446 **Competing interests:** Authors declare that they have no competing interests.

447

448



450

451

452

453

454

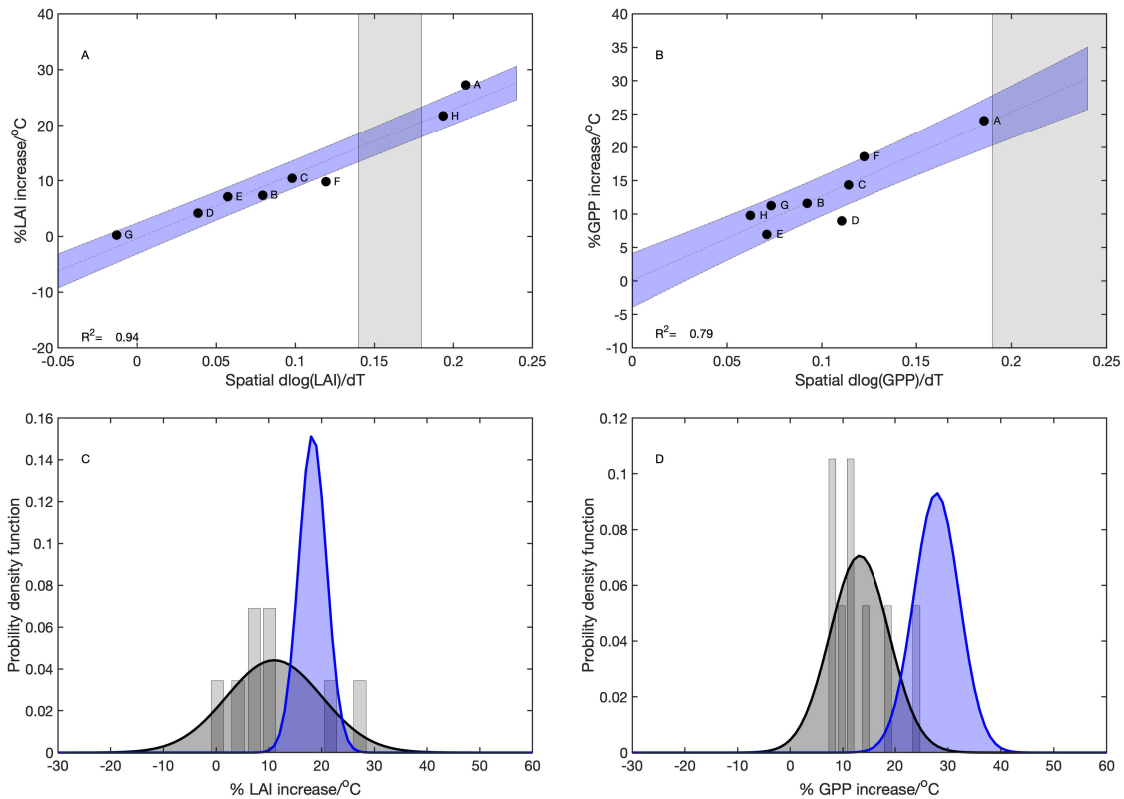
455

456

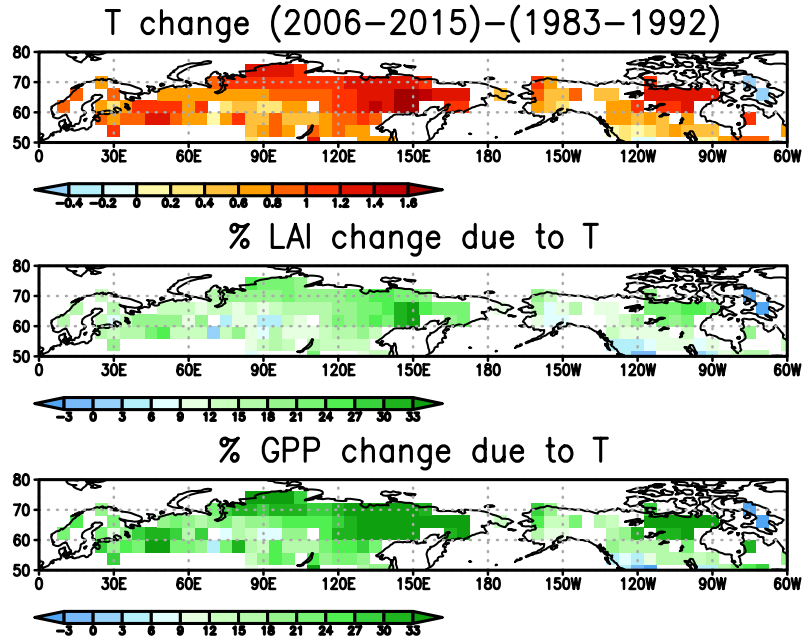
457

458

Figure 1 The spatial sensitivity of growing season LAI and GPP to temperature does not change over the 100-year simulations by TRENDY. The ensemble model mean underestimates the sensitivity diagnosed from observations. A. The spatial sensitivity of growing season LAI to temperature for the TRENDY ensemble models (A-H), model mean (mean-mod), and the LAI (OBS). B. The spatial sensitivity of growing season GPP to temperature for the TRENDY ensemble models (A-H), model mean (mean-mod), and the GPP (OBS) (unit: $gC/m^2/day/^\circ C$). The model names corresponding to each model ID is listed in Table S1. The width of the bars represents how well correlated LAI and GPP are with temperature.

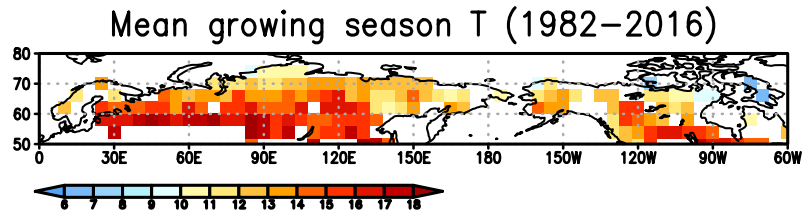


459
 460 **Figure 2 An emergent constraint on the percentage changes of LAI and GPP due to**
 461 **temperature increase since 1901 with the corresponding observed spatial sensitivity to**
 462 **temperature over the high latitude northern forests. A. The relationship between the modeled**
 463 **spatial sensitivity of LAI to temperature and the modeled temporal sensitivity of LAI increase due**
 464 **to temperature alone (γ_G^{LAI}). B. The relationship between the modeled spatial sensitivity of GPP**
 465 **to temperature and the modeled temporal sensitivity of GPP increase due to temperature alone**
 466 **(γ_G^{GPP}). C. The unconstrained probability density function distribution of γ_G^{LAI} across models (grey**
 467 **bars), which assumes that all of the TRENDY models have equal possibility and that their**
 468 **distribution is Gaussian. The blue area represents the conditional probability distribution derived**
 469 **by applying the constraint from A to the across-model relationship. D. The unconstrained**
 470 **probability density function distribution of γ_G^{GPP} across models (grey bars), which assumes that all**
 471 **of the TRENDY models have equal possibility and their distribution is Gaussian. The blue area**
 472 **represents the conditional probability distribution derived by applying the constraint from B to the**
 473 **across-model relationship. The unconstrained γ_G^{LAI} is $11.0 \pm 9.0\% / ^\circ\text{C}$ (1σ), and the constrained**
 474 **γ_{obs}^{LAI} is $18.3 \pm 2.6\% / ^\circ\text{C}$. The emergent constrained reduced the uncertainty by 70%. The**
 475 **unconstrained γ_G^{GPP} is $13.2 \pm 5.6\% / ^\circ\text{C}$ the constrained γ_{obs}^{GPP} is $27.8 \pm 4.3\% / ^\circ\text{C}$. The emergent**
 476 **constrained reduced the uncertainty by 24%.**
 477



478
 479 Figure 3 The observational-constrained carbon-climate feedback factors γ_{obs}^{LAI} and γ_{obs}^{GPP}
 480 implies that temperature increase between 2006-2015 and 1983-1992 contributed to 9-27%
 481 increase of LAI and 12-35% increase in GPP over most of the region. A. The growing season
 482 mean temperature change between 2006-2015 and 1983-1992 (temperature data is based on ERA-
 483 5); B. Percentage change of LAI due to temperature increase calculated from γ_{obs}^{LAI} ; C. Percentage
 484 change of GPP due to temperature increase calculated from γ_{obs}^{GPP} .
 485
 486
 487

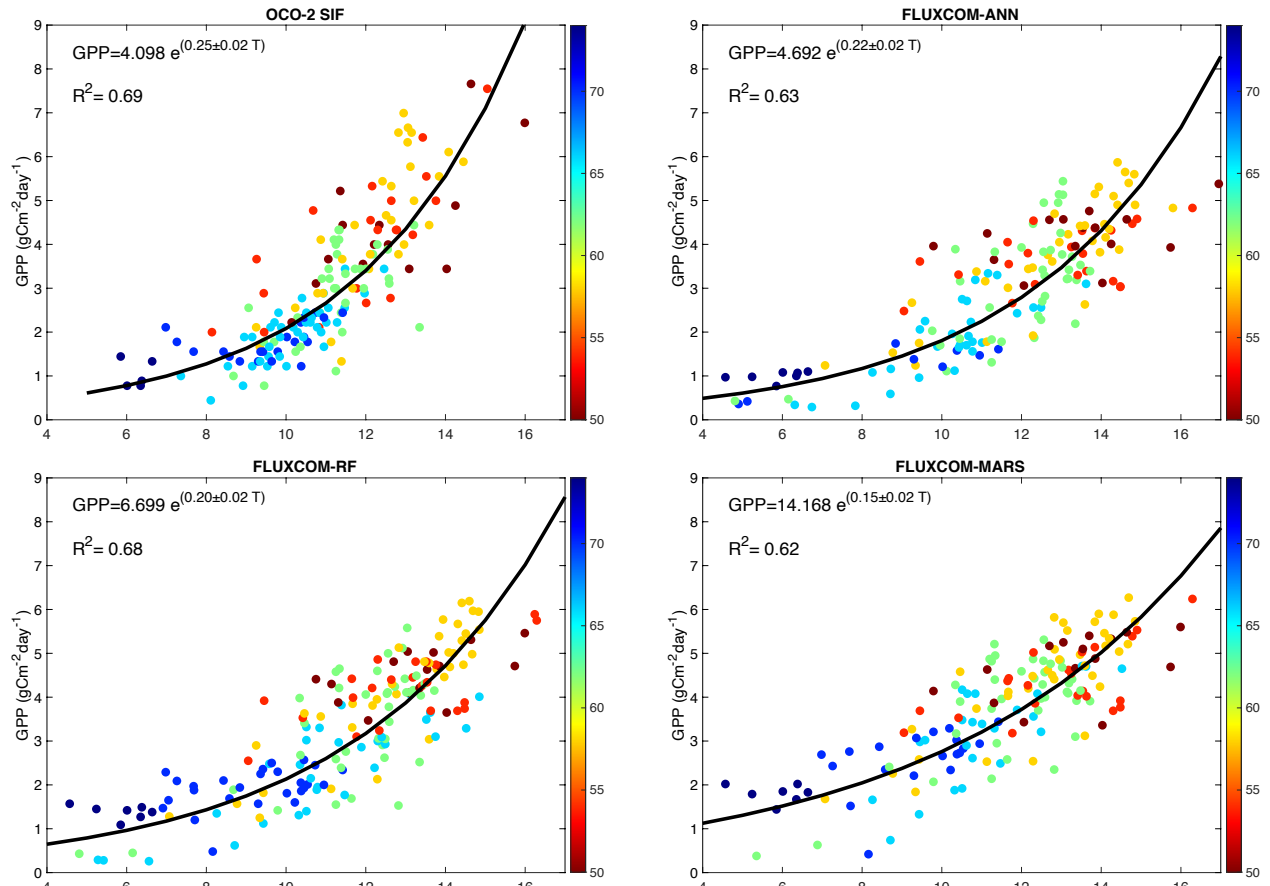
488



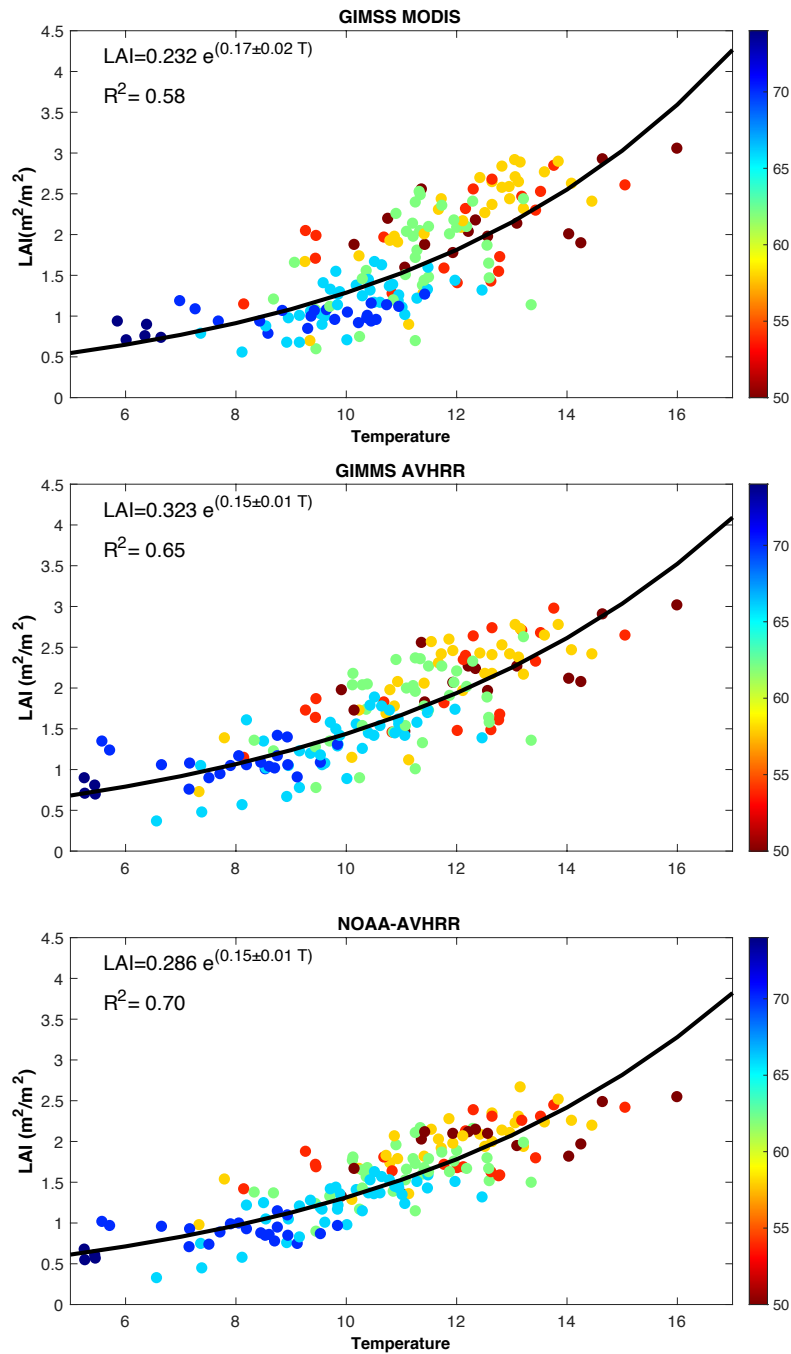
489

490 Extended Data Fig. 1 Mean growing season temperature between 1982 and 2016 (unit: °C) over
491 grids (4° (latitude) x 5° (longitude)) with tree cover fraction larger than 40%.

492

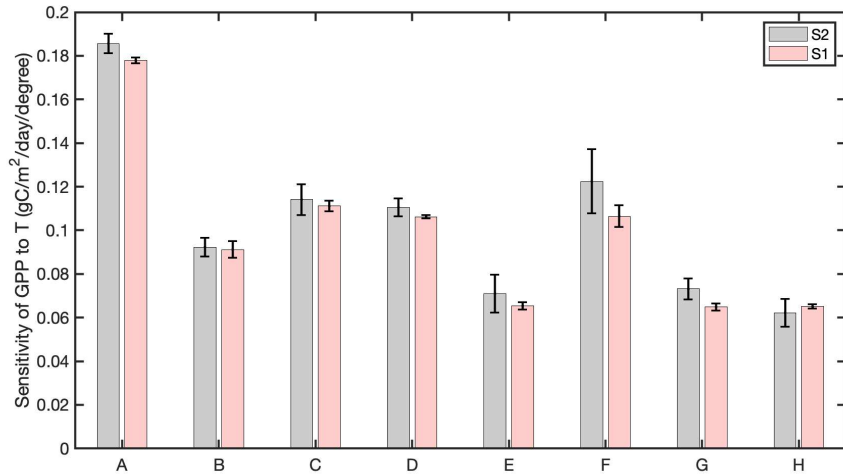
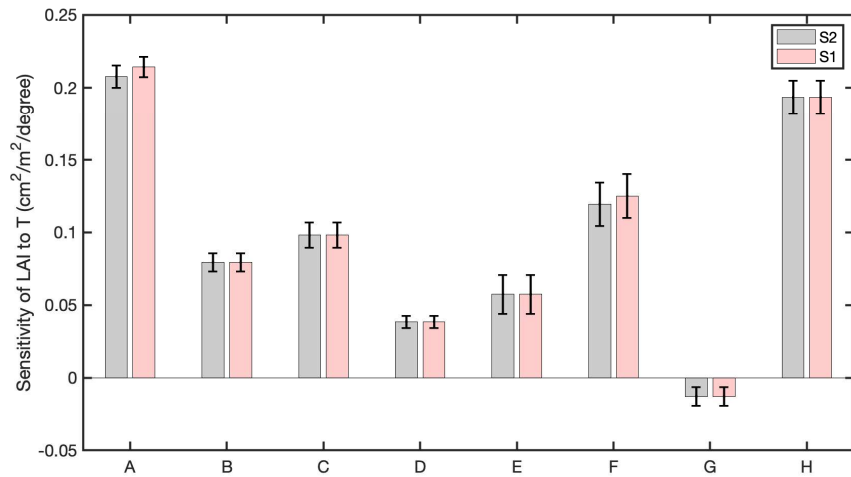


493
 494 Extended Data Fig. 2 The spatial sensitivity of GPP to temperature. The points are those with at
 495 least 40% tree cover north of 50°N. A. OCO-2 SIF -constrained GPP; B. FLUXCOM GPP based on
 496 ANN algorithm; C. FLUXCOM GPP based on random forest (RF); D. FLUXCOM GPP based on MARS
 497 algorithm.
 498
 499



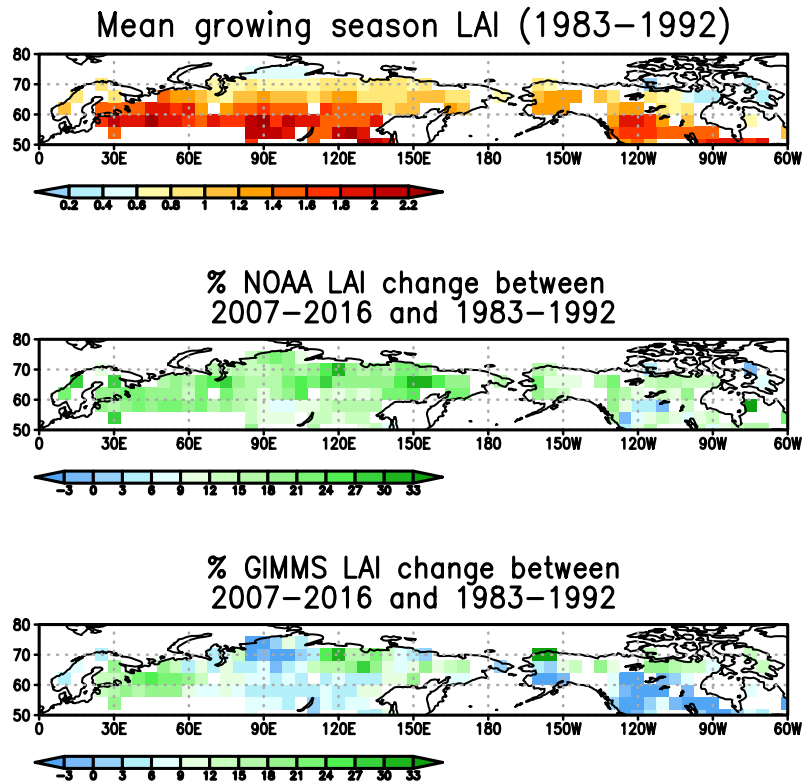
500
 501
 502
 503
 504
 505

Extended Data Fig. 3 The spatial sensitivity of observed LAI to temperature. The points are those with at least 40% tree cover north of 50°N. The color bar represents latitudes of those points. A: GIMSS iMODIS LAI; B: GIMSS AVHRR LAI; C: NOAA AVHRR LAI;



506
 507 Extended Data Fig. 4 The S1 runs and S2 runs have similar magnitude of spatial sensitivity of
 508 growing season LAI (A) and GPP (B) to temperature. The error bars are the standard deviations
 509 of the corresponding spatial sensitivity among the 10 groups in each model. The model names
 510 corresponding to each model ID are listed in Extended Data Table 1.

511
 512
 513
 514
 515
 516
 517
 518
 519
 520



521
 522
 523
 524
 525
 526
 527
 528

Extended Data Fig. 5 The mean growing season LAI between 1983 and 1992 (A) and the actual percentage changes of LAI between 2007-2016 and 1983-1992 based on NOAA AVHRR LAI (B) and GIMMS AVHRR LAI products (C) respectively.

529

530 Extended Data Table 1 Summary of TRENDY v6 models. Only models that have monthly GPP
 531 and LAI from both S1 and S2 runs, and either $R^2(\text{LAI}, T)$ or $R^2(\text{GPP}, T)$ larger than 0.2 were
 532 selected. For models without land cover fraction information, the compressed IGBP data from
 533 MODIS was used to identify grid with at least 40% tree cover.

	ID	$R^2(\text{LAI}, T)$	$R^2(\text{GPP}, T)$	Selected or not	Land Cover	Reference
VEGAS	A	0.7	0.7	Yes	MODIS	Zeng et al., 2005 ³⁷
ORCHIDEE	B	0.3	0.6	Yes	ORCHIDEE	Krinner et al., 2005 ³⁸
ORCHIDEE-MICT	C	0.3	0.4	Yes	ORCHIDEE-MICT	Guimberteau et al., 2017 ³⁹
ISAM	D	0.1	0.7	Yes	ISAM	Jain et al., 2013 ⁴⁰
CLM4.5	E	0.2	0.2	Yes	MODIS	Oleson et al., 2013
CLASS-CTEM	F	0.1	0.1	Yes	CLASS-CTEM	Melton et al., 2016 ⁴¹
JSBACH	G	0.01	0.3	Yes	JSBACH	Reick et al., 2013 ⁴²
LPX	H	0.6	0.2	Yes	MODIS	Keller et al., 2017 ⁴³
JULES	N/A	0.0	0.0	$R^2(\text{LAI}, T)=0.0$	N/A	Clark et al., 2011 ⁴⁴
LPJ-hyde	N/A	N/A	0.2	no monthly LAI	N/A	Sitch et al., 2003 ⁴⁵
LPJ-GUESS	N/A	0.0	0.1	$R^2(\text{LAI}, T)=0.0$	N/A	Smith et al., 2014 ⁴⁶
VISIT	N/A	0.0	0.0	$R^2(\text{GPP}, T)=0.0$	N/A	Kato et al., 2013 ⁴⁷
CABLE	N/A	N/A	N/A	No S2 run	N/A	Haverd et al., 2017 ⁴⁸
DLEM	N/A	N/A	N/A	No LAI	N/A	Tian et al., 2015 ⁴⁹

534

535